Superconductivity drives magnetism in δ-doped La_2CuO_4

A. Suter,[1,*] G. Logvenov,[2] A. V. Boris,[2] F. Baiutti,[2] F. Wrobel,[2] L. Howald,[3] E. Stilp,[1,4]
Z. Salman,[1] T. Prokscha,[1] and B. Keimer[2]

[1]*Laboratory for Muon Spin Spectroscopy, Paul Scherrer Institute, CH-5232 Villigen PSI, Switzerland*
[2]*Max Planck Institute for Solid State Research, Heisenbergstrasse 1, 70569 Stuttgart, Germany*
[3]*SLS, Paul Scherrer Institute, CH-5232 Villigen PSI, Switzerland*
[4]*Materials for Energy Conversion, Empa, CH-8600 Dübendorf, Switzerland*

(Received 23 June 2017; revised manuscript received 23 February 2018; published 27 April 2018)

Understanding the interplay between different orders in a solid is a key challenge in highly correlated electronic systems. In real systems this is even more difficult since disorder can have strong influence on the subtle balance between these orders and thus can obscure the interpretation of the observed physical properties. Here we present a study on δ-doped La_2CuO_4 (δ-LCO_N) superlattices. By means of molecular beam epitaxy whole LaO_2 layers were periodically replaced by SrO_2 layers, providing a charge reservoir yet reducing the level of disorder typically present in doped cuprates to an absolute minimum. The induced superconductivity and its interplay with the antiferromagnetic order is studied by means of low-energy muon spin rotation. We find a quasi-two-dimensional superconducting state which couples to the antiferromagnetic order in a nontrivial way. Below the superconducting transition temperature, the magnetic volume fraction increases strongly. The reason could be a charge redistribution of the free carriers due to the opening of the superconducting gap which is possible due to the close proximity and low disorder between the different ordered regions.

DOI: 10.1103/PhysRevB.97.134522

I. INTRODUCTION

The copper oxide–based high-temperature superconductors (cuprates) exhibit rich and complex physics [1]. Strong electron correlations drive the parent compounds into an insulating, antiferromagnetic ground state. Upon sufficiently high doping of the copper oxide planes by electrons or holes, superconductivity appears. Still, even for doping levels where the highest superconducting transition temperature T_c is reached, short-range antiferromagnetic correlations persist. In some cuprates, the competition between superconducting and magnetic orders causes a tendency towards electronic phase separation, especially on the underdoped side of the phase diagram. The phase coexistence of superconductivity and antiferromagnetic stripe order in the $La_{2-x-y}M_ySr_xCuO_4$ family was observed at finite temperatures by neutron scattering for M = Nd [2] and muon spin rotation (μSR)/NMR for M = Eu [3]. Subsequent intense theoretical efforts showed (Ref. [4] and references therein) that within the t-J model, there is close competition between uniform d-wave superconductivity and various stripe states and the real ground state is very susceptible to disorder. One source of disorder in the cuprates is the dopant atoms, which adds another level of complexity [5]. In this respect, superoxygenated $La_2CuO_{4+\delta}$ [6,7] is an interesting family. There the excess oxygen intercalates in a self-organized manner into the structure and thus forms antiferromagnetic and superconducting regions [8]. Quite remarkably, magnetism and superconductivity set in at the same temperature, independent of the Sr content and characteristic of optimally doped oxygen-stoichiometric $La_{2-x}Sr_xCuO_{4+\delta}$ [9]. Furthermore, the concomitant magnetic propagation vector remains consistent with that of the stripe-ordered cuprates.

II. SAMPLES

In this paper we demonstrate an approach to dope La_2CuO_4. Rather than randomly substituting lanthanum by strontium, which leads to microscale disorder, we replace single planes of LaO with SrO dopant planes using atomic layer-by-layer molecular beam epitaxy [10,11]. This allows much better control over the disorder compared to bulk $La_{2-x}Sr_xCuO_{4+\delta}$ and, at the same time, gives another degree of freedom, namely, the separation of the charge reservoirs. In this way a system on the mesoscopic scale can be engineered, allowing us to tune the interplay between superconducting and antiferromagnetic ground states. Figure 1 depicts a sketch of such a superlattice which we call δ-doped La_2CuO_4. The distance between SrO dopant layers is labeled by N, which is the number of half unit cells separating them, and hence, we will abbreviate this family as δ-LCO_N.

III. RESULTS AND ANALYSIS

Utilizing low-energy muon spin rotation techniques (LE-μSR), we find a nontrivial enhancement of the magnetic volume fraction below the superconducting transition of the

*Corresponding author: andreas.suter@psi.ch

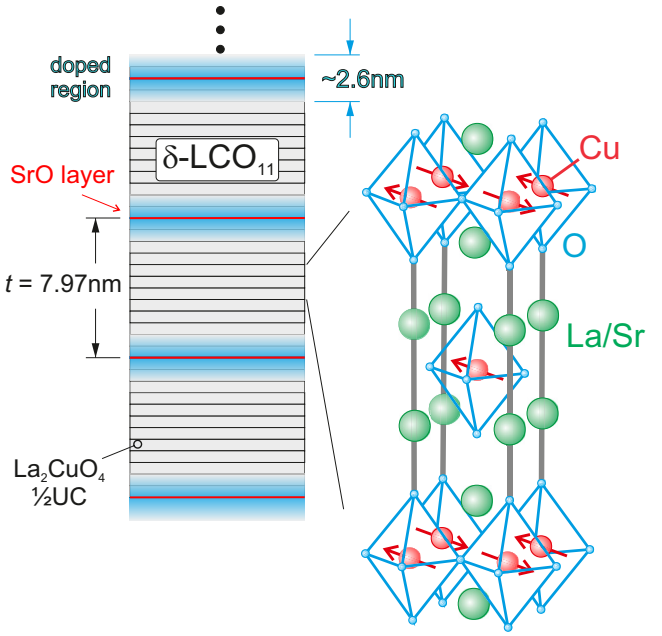

FIG. 1. Sketch of δ-doped La_2CuO_4, here δ-$LCO_{N=11}$. Starting from La_2CuO_4, a superlattice is formed by replacing single layers of LaO with SrO planes. The general formula can be written as $R \times$ [SrO-LaO-CuO_2 + $N \times$ LaO-LaO-CuO_2]; that is, the natural counting is given in half crystallographic unit cells. R is adjusted such that the overall thickness of the δ-LCO_N superlattices is about 40 nm. The negatively charged interface region around the SrO layer will lead to a layered charge distribution throughout the superlattice, as depicted with the light blue layers. An in-depth study about the structure and charge distribution within the δ-LCO_N superlattices is found in Ref. [10]. The crystal structure on the right sketches undoped La_2CuO_4. Each copper ion (red) is in a spin-1/2, $3d_{x^2-y^2}$ configuration with a strong antiferromagnetic in-plane coupling and a much weaker out-of-plane coupling which leads, in bulk, to a Néel temperature of about $T_N = 325$ K [12].

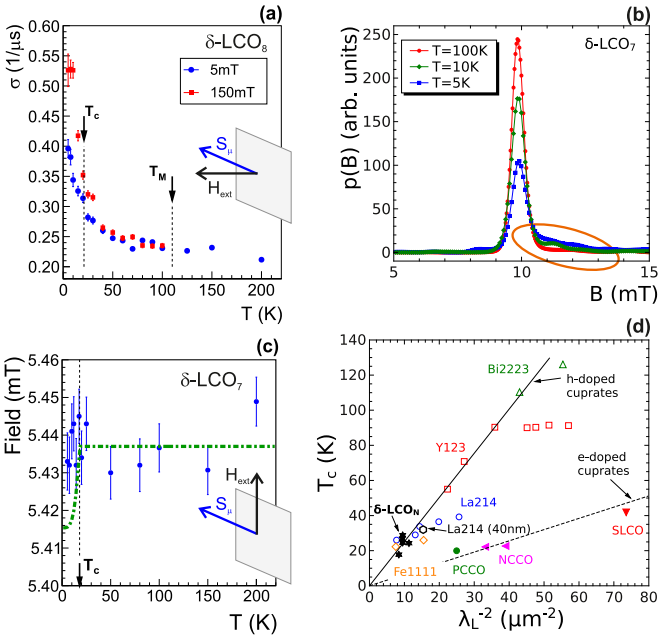

FIG. 2. (a) The muon depolarization rate $\sigma(T)$ as a function of the temperature. It is obtained from field-cooling measurements with the applied magnetic field H_{ext} perpendicular to the δ-LCO_N superlattice film plane. (b) The magnetic field probability distribution (z components $\parallel$ to H_{ext}) of the vortex state. (c) The temperature dependence of the measured magnetic field in the Meissner state. The green dash-dotted line shows the expected temperature dependence in the Meissner state taking into account λ_L obtained from the vortex state and assuming a screening throughout the film. (d) The Uemura plot with the δ-LCO_N results and an optimally doped $La_{2-x}Sr_xCuO_4$ film with a thickness of 40 nm. Data for the other systems are from Ref. [24] and references therein.

δ-LCO_N superlattices that has a striking resemblance to bulk superoxygenated $La_{2-x}Sr_xCuO_{4+\delta}$. Furthermore, it is shown that the superfluid density of δ-LCO_N is in line with the Uemura relation [13]; namely, the superfluid density is anomalously small and proportional to T_c on the underdoped side. LE-μSR allows us to study internal magnetic field distributions of any material [14] and thus is very well suited to investigating systems with a complex interplay between magnetic and superconducting ground states. By tuning the implantation energy of the positively charged muon (μ^+), the stopping range can be varied between 5 and 300 nm (Appendix B). For this study an implantation energy E_{impl} was chosen such that the full muon beam stops in the center of the superlattice. In order to obtain information about the superconducting state it is possible to study either the vortex state or the Meissner state. From measurements in the vortex state the magnetic field distribution is obtained. For a regular vortex lattice, the second moment of the magnetic field distribution is proportional to the muon depolarization rate $\sigma(T)$ and directly related to the magnetic penetration depth $\lambda(T)$ as [15]

$$\left(\frac{\sigma_{sc}(T)}{\gamma_\mu}\right)^2 = 0.00371\,\frac{\Phi_0^2}{\lambda(T)^4}, \qquad (1)$$

where γ_μ is the muon gyromagnetic ratio, $\sigma_{sc} = \sqrt{\sigma(T)^2 - \sigma(T > T_c)^2}$, and $\Phi_0 = 2.067 \times 10^{-15}(\mathrm{T\,m^2})$ is the flux quantum. Equation (1) is an approximation, and a more elaborate calculation leads to a magnetic-field-dependent $\sigma_{sc}(T,B)$ [16]. However, $\sigma_{sc}(T,B)$ versus B shows a very broad maximum, and field-dependent measurements (see Fig. 11 in Appendix D) show that $\sigma_{sc}(B)$ is in the field range of $40\,\mathrm{mT} \leqslant \mu_0 H_{ext} \leqslant 150\,\mathrm{mT}$ essentially constant. Figure 2(a) shows the temperature dependence of σ due to the vortex state, and Fig. 2(b) presents the magnetic field probability distribution (z components) of the vortex state given by the Fourier transform of the muon spin polarization function [see Eq. (B3)]. The marked high-field shoulder is typical for a regular vortex lattice. Since the film thickness, $d \simeq 40$ nm, is small compared to the London penetration depth λ_L, $\lambda(T)$ in Eq. (1) represents an effective magnetic penetration depth [17]. The relation between them is approximately given by $\lambda_L^2(T) \simeq c_0\lambda(T)d$, with $c_0 = 1/2$. Measurements on optimally doped $La_{2-x}Sr_xCuO_4$ with $d = 40$ nm were scaled such that we obtained the bulk data, resulting in $c_0 = 4.3$. Currently, it is not clear why c_0 from the scaling is about one order of magnitude larger compared to the simple theoretical estimate. Since the theoretical estimate is obtained for the bulk, i.e., ignoring any boundary conditions likely to be relevant in the context presented here, we chose the experimentally

determined scaling factor to estimate λ_L for the superlattices. For the chosen geometry λ_L is equal to the in-plane magnetic penetration depth λ_{ab}. The Uemura plot in Fig. 2(d) shows that the δ-LCO_N superlattices are in line with the hole-doped cuprates.

Assuming a homogeneous superconducting state, measurements in the Meissner state (zero-field cooled, $H_{ext} < H_{c1}$ [18]) should show a corresponding magnetic field shift as depicted by the dash-dotted line in Fig. 2(c). The absence of any field shift in the Meissner state demonstrates that superconductivity is layered in nature and likely localized around the charged SrO layers. This is in line with the measured charge distribution in δ-LCO_N [10].

In metal-insulator superlattices of the form $R \times [3 \times La_{1.55}Sr_{0.45}CuO_4 + N \times La_2CuO_4]$ the charge-transfer effects throughout the superlattices were modeled quantitatively [19,20]. This is possible since the chemical potential as a function of Sr doping in $La_{2-x}Sr_xCuO_4$ has been experimentally determined [21]. The result shows that superconducting layers along the interfaces form with an extent of about one unit cell (UC). As for the δ-LCO_N superlattices, the Josephson coupling in the vortex state breaks down [field geometry as in Fig. 2(a)], and the Meissner state is suppressed [as in Fig. 2(c)]. These findings are further supported by the temperature dependence of $\sigma(T)$, which does not follow the expected behavior $\sigma(T) \propto [1 - (T/T_c)^r]$, $r \simeq 2, \ldots, 6$.

The situation is very reminiscent of the case of intercalated Bi2212 and Bi2202 [22], in which the interlayer spacing between adjacent CuO_2 layers was tuned by intercalating guest molecules. Above a critical separation the Josephson coupling between adjacent layers becomes too weak, and only the dipole-dipole interaction remains to align the pancake vortices. The σ versus T behavior found there is essentially identical to what is shown in Fig. 2(a). The superconducting state of the δ-LCO_N superlattices can be summarized such that superconducting layers are forming rather localized around the SrO layers. The distance between these quasi-two-dimensional superconducting layers range from ~2.6 nm for δ-LCO_3 to ~7.9 nm for δ-LCO_{11}; thus, the Josephson coupling between layers is essentially suppressed, and only dipolar interaction between vortices can stabilize the vortex lattice. Therefore, the superconducting ground state is extremely anisotropic. A very recent infrared spectroscopy study of charge dynamics in δ-LCO_N confirms that the superconducting state in this system is essentially two-dimensional [23].

μSR is a well-established method to study magnetic systems [25]. The reasons are that the ground state can be studied in zero applied magnetic field, and a sensitivity of about $10^{-3}\mu_B$ per unit cell is reached. Figures 3(a)–3(c) show the time evolution of the muon spin asymmetry, $A(t) = A_0\,P(t)/P(0)$. A_0 is the instrumental asymmetry, and $P(t)$ is the muon spin polarization of the time ensemble (see Sec. B 1 a). For the δ-LCO_3 superlattice $A(t)$ shows a Gaussian-like time evolution typical of a paramagnetic state in which the loss of the polarization is governed solely by the dephasing of the muon spin ensemble due to the quasistatic nuclear magnetic dipole fields [26]. The very weak temperature dependence of $A(t)$ is an indication of the gradual slowing down of the high-frequency short-range magnetic correlation still present in the system. These zero-field results show that a SrO-layer

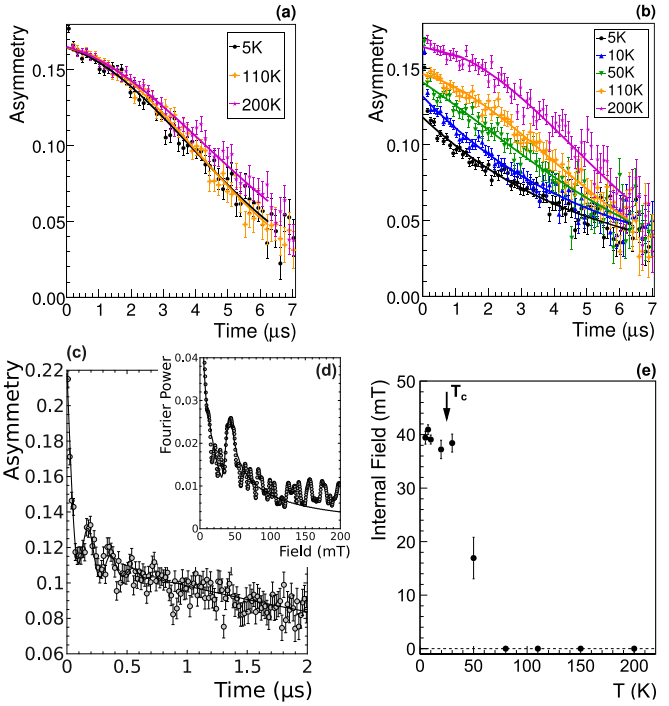

FIG. 3. Zero-field LE-μSR data for δ-LCO_3 and δ-LCO_{11}. The measured asymmetry $A(t)$ is proportional to the muon spin polarization $P(t)$. (a) and (b) Asymmetry time spectra of the δ-LCO_3 and δ-LCO_{11} superlattices, respectively, measured at various temperatures. (c) The short time asymmetry spectrum measured at $T = 5$ K of δ-LCO_{11}, where a clear spontaneous zero-field precession is visible; (d) its Fourier transform. (e) The temperature dependence of the internal magnetic field for δ-LCO_{11} at the muon stopping site.

separation of ~2.6 nm is close enough to fully suppress the antiferromagnetic ground state of the La_2CuO_4 layers due to charge transfer. Essentially, δ-LCO_3 behaves as a metal with short-range antiferromagnetic correlations.

δ-LCO_{11} shows a drastically different behavior. The full time spectra shown in Fig. 3(b) change from an initially Gaussian-like behavior at high temperature to an exponential one at low temperature. At short times and low enough temperature, spontaneous zero-field precession is found [see Fig. 3(c)]. This shows that δ-LCO_{11}, different from δ-LCO_3, undergoes an antiferromagnetic transition. To be able to quantify the changes in the asymmetry spectra, the following zero-field fit model was used:

$$\begin{aligned} A(t) &= A_0 P(t)/P(0)|_{ZF} \\ &= A_1\left(\tfrac{1}{3} + \tfrac{2}{3}\{1-(\Delta t)^2\}\exp\left[-\tfrac{1}{2}(\Delta t)^2\right]\right)e^{-\Lambda t} \\ &\quad + A_{osc}\, j_0(\gamma_\mu B_{int} t + \phi)\, e^{-(\sigma_{osc} t)^2/2}. \end{aligned} \tag{2}$$

Since the muon stopping distribution covers the whole superlattice, the asymmetry spectrum $A(t)$ will be a superposition of muons experiencing a paramagnetic surrounding (close to the SrO doping layers) and muons stopping in an antiferromagnetic surrounding (far from the SrO layers). The first term describes the paramagnetic response of the sample. Δ is the width of the magnetic field distribution due to nuclear dipoles, and Λ describes the slowing down of high-frequency

TABLE I. Estimates of the magnetic and superconducting thicknesses. The second and third columns give the magnetic volume fraction at T_c and zero temperature, respectively. The superlattice repetition length is $d_N = (N+1) \times \mathrm{UC}/2$, with UC = 1.32 nm. The magnetic layer thickness is therefore defined as $d_M(T) = f_M(T) d_N$. An *upper limit* for the superconducting layer thickness is thus $d_S(0) = d_N - d_M(0)$. The last two columns give the T_c of the superlattices and λ_L^{-2}. For λ_L^{-2} two errors are given; the first is a statistical error estimate, whereas the second is an estimate for the systematic errors.

N	$f_M(T_c)$	$f_M(0)$	d_N (nm)	$d_M(T_c)$ (nm)	$d_M(0)$ (nm)	$d_S(0)$ (nm)	T_c (K)	λ_L^{-2} (μm^{-2})
3	0	0	2.64	0	0	2.64	28.8	9.5(3)(2)
7	0.13	0.5	5.28	0.69	2.64	2.64	17.8	8.4(3)(4)
8	0.27	0.7	5.94	1.6	4.16	1.78	24.3	11.3(4)(7)
9	0.10	0.4	6.60	0.66	2.64	3.96	26.8	9.4(2)(5)
11	0.32	0.54	7.92	2.53	4.28	3.64	24.6	9.5(3)(5)

short-range magnetic correlations. The second term describes the regions which are antiferromagnetically ordered. The zero-field precession signal is well described by a zero-order spherical Bessel function. For a more detailed discussion of Eq. (2) see Sec. B 1 a. The value of the internal magnetic field B_{int} is a very sensitive measure of the doping level in $La_{2-x}Sr_xCuO_4$ [27,28]. We find $B_{\mathrm{int}}(T \to 0) = 40(2)$ mT, which allows us to estimate an upper doping level in the antiferromagnetic regions of $x < 0.01$. Furthermore, this value shows that the full electronic Cu moment of about $0.64\mu_B$ is present in the antiferromagnetic state. The zero-field time spectra and temperature dependencies of the asymmetries of δ-LCO_N, $N = 7,8,9$, are found in Appendix C. The loss of the temperature-dependent paramagnetic asymmetry $1 - A_1(T)/A_0$ reflects the growth of the magnetic volume fraction. In order to quantify this effect, weak transverse field measurements (wTF) were carried out, which allows us to measure the magnetic volume fraction f_M in a precise manner. The long-lived oscillation amplitude in the wTF asymmetry represents muons in a non- or paramagnetic environment. Figure 4 shows a typical wTF measurement in an applied field of $\mu_0 H_{\mathrm{ext}} = 5$ mT. The data were fitted to

$$A(t) = A_0 P(t)/P(0)|_{\mathrm{wTF}} = A_T e^{-(\sigma t)^2/2} \cos(\gamma_\mu [\mu_0 H_{\mathrm{ext}}] t + \phi) + A_L \cos(\phi). \quad (3)$$

The magnetic volume fraction is given by $f_M = 1 - A_T/A_0$. For all para- and diamagnetic states $A_L \equiv 0$. Therefore, the finite value of A_L found below T_M for $T = 5$ K, depicted in Fig. 9, clearly demonstrates the presence of a magnetic ground state. The low-temperature magnetic volume fraction allows us to estimate the superconducting layer thickness. Assuming that the superlattices are laterally homogeneous, with no stripelike electron patterns within the superconducting layer, magnetic and superconducting layer thicknesses can be estimated, as presented in Table I. It shows that the upper limit for the superconducting layer thickness $d_S(0) \simeq 2$–4 nm, as sketched in Fig. 1. This value is consistent with the dopant profile in δ-LCO_N as measured by high-resolution and analytical scanning transmission electron microscopy [11], and hence, it is not too surprising that δ-LCO_3 shows only marginal signs of magnetism since $d_N \simeq d_S(0)$.

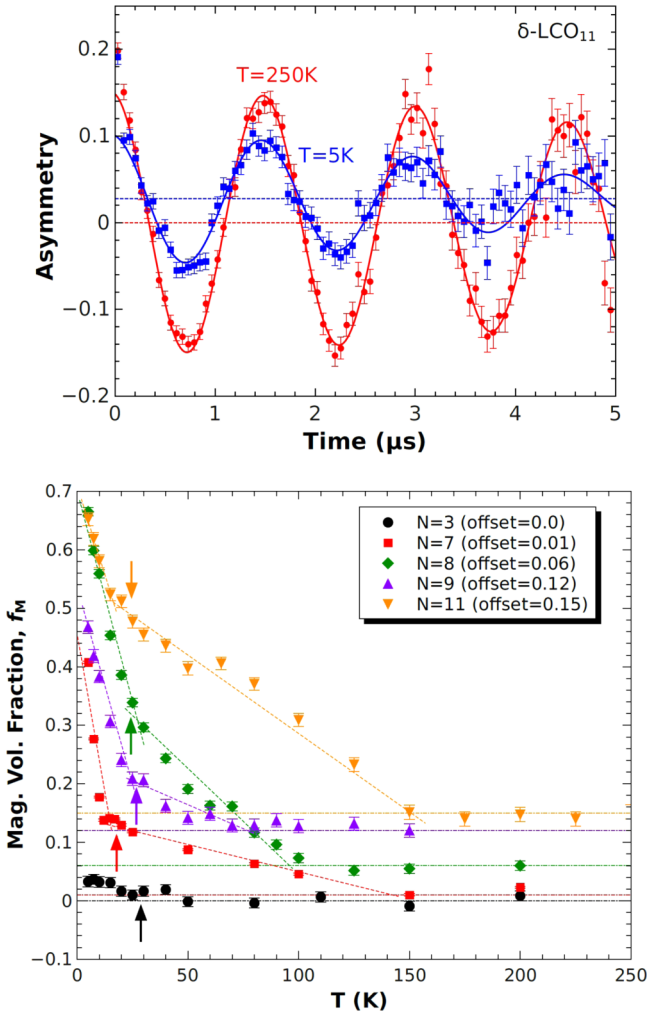

FIG. 4. Top: weak transverse field asymmetry time spectra for δ-LCO_{11}, measured in a field of $\mu_0 H_{\mathrm{ext}} = 5$ mT. The red data set is measured in the paramagnetic phase at $T = 250$ K, whereas the blue data set is measured at $T = 5$ K. The low-temperature data show an asymmetry offset A_L, which demonstrates that a fraction of muons samples a magnetic surrounding. Bottom: the magnetic volume fractions $f_M(T)$ versus temperature. All measured δ-LCO_N superlattices show a clear change in slope at T_c, indicated by the arrows; that is, the magnetic regions increase faster when the adjacent metallic layers become superconducting. For clarity, the data sets for $f_M(T)$ for the different superlattices are shifted with respect to each other.

A closer look at the temperature dependence of $f_M(T)$ (Fig. 4) reveals a rather unusual behavior. Typically, $f_M(T)$ shows a sharp upturn at T_M as found in various copper- and iron-based superconductors [9,28–30]. In contrast, for all δ-LCO_N, $f_M(T)$ increases very gradually, almost linearly, when the temperature is lowered. However, at exactly T_c there is a clear trend change; df_M/dT is strongly increasing. As shown in Appendix D, this behavior is also present when the external magnetic field H_{ext} is applied parallel to the superlattice layers, thus ruling out that the observed effect is related to the formation of a vortex lattice in the superconducting state. This observation suggests that the magnetic and superconducting ground states are coupled.

IV. DISCUSSION

This strongly resembles trends found in $La_{2-x}Sr_xCuO_{4+\delta}$, where df_M/dT also shows a clear trend change at T_c [9]. In the superoxygenated $La_2CuO_{4+\delta}/La_{2-x}Sr_xCuO_{4+\delta}$ families the excess oxygen is found interstitially and leads to a superstructure [6,7]. Yet there are also marked differences from the δ-LCO_N family. In δ-LCO_N the magnetic onset temperature does not coincide with T_c and, e.g., for δ-LCO_{11} is as high as $T_M = 150\,K \simeq 6T_c$. Furthermore, the magnetic structures of $La_2CuO_{4+\delta}$ and $La_{2-x}Sr_xCuO_{4+\delta}$ are stripe-phase-like, whereas the zero-field spectra for δ-$LCO_{9,11}$ suggest an antiferromagnetic ground state. Whether these differences are caused by the inevitable disorder present in the superoxygenated $La_2CuO_{4+\delta}/La_{2-x}Sr_xCuO_{4+\delta}$ families is not clear at this stage.

On the theoretical side there has been little work published which tries to establish a coupling of the superconducting and magnetic orders. In Ref. [31] the authors discuss, in the context of stripe formation, the coupling between incommensurate antiferromagnetic and superconducting orders in terms of the thermodynamics of fluid mixtures. They confirm that $f_M(T)$ may grow in the superconducting state, although not giving a microscopic explanation of the simultaneous onset of magnetism and superconductivity, $T_M \approx T_c$. Further experimental and theoretical development is necessary in order to gain a comprehensive understanding of the superconductivity-induced long-range magnetic order in the La_2CuO_4-based superconductors. A possible explanation of the trend change in $f_M(T)$ at T_c could be related to charge redistribution between different phases caused by a lowering of the chemical potential upon the opening of the superconducting gap in the superconducting phase; a mechanism similar to that discussed for the superconductivity-induced charge redistributions between different planes in the cuprates [32] or between different electronic bands in the multigap Fe-based superconductors [33]. In δ-LCO_N, as soon as the regions around the SrO layers turn superconducting, for holes residing in the antiferromagnetic regions, it would energetically be favorable to migrate into the "active" superconducting layers below T_c, thus "cleaning up" the antiferromagnetic layers and leading to a stronger increase in f_M. This could be possible in these systems due to the mesoscopic proximity. Whatever explanation proves correct, the advantage of systems such as the presented δ-LCO_N over the homogeneously doped bulk cuprates is the much higher level of control over the spatial parameters in these systems. Further high-resolution transmission electron microscopy and resonant x-ray experiments are necessary to verify the correlation of the out-of-plane charge distribution and associated structural distortion [11] with the onset of the superconductivity in δ-LCO_N in order to shed light on the intriguing interplay between superconductivity and long-range antiferromagnetic order in the La_2CuO_4-based superconductors.

ACKNOWLEDGMENTS

We gratefully acknowledge S. A. Kivelson, J. Tranquada, C. Bernhard, and I. Bozovich for fruitful discussions.

APPENDIX A: SAMPLE FABRICATION AND CHARACTERIZATION

Sr-δ-doped La_2CuO_4 superlattices were synthesized on $LaSrAlO_4$ (001) substrates (Crystec GmbH) using an atomic layer-by-layer (ALL) oxide molecular beam epitaxy system (DCA Instrument) [1]. In these superlattices LaO atomic layers were substituted by SrO layers with predefined periodicity. In this method the constituent elements (Sr, La, and Cu) were deposited one atomic layer at a time from separate evaporation sources. Flux calibration was routinely carried out prior to each sample deposition using a quartz crystal microbalance, whereas the growth process was monitored by employing *in situ* reflection high-energy electron diffraction. The deposition parameters were as follows: substrate temperature $T_s \approx 600\,^\circ C$ according to an IR pyrometer and total pressure of the gas mixture delivered from the ozone delivery system (ozone, atomic oxygen, and molecular oxygen) $p \approx 1.5 \times 10^{-5}$ Torr. After the growth, the films were cooled down under the same atmospheric conditions to $\sim 200\,^\circ C$ and then in high vacuum in order to remove possible interstitial oxygen from the structure. Every superlattice was characterized *ex situ* by atomic force microscopy, x-ray diffraction, and the temperature dependence of the resistivity and magnetic susceptibility measurements. Selected samples were investigated using high-resolution scanning transmission electron microscopy. Detailed information concerning the superconducting properties, Sr distribution, locus of superconductivity, oxygen octahedron distortions, and mechanism of Sr segregation can be found in Refs. [10,11,34]. Figure 5 depicts the T_c versus Sr doping x diagram for bulk $La_{2-x}Sr_xCuO_4$, together with the T_c values of the measured δ-LCO_N samples. The formal Sr-doping level for the δ-LCO_N samples is calculated as $x = 1/(N+1)$.

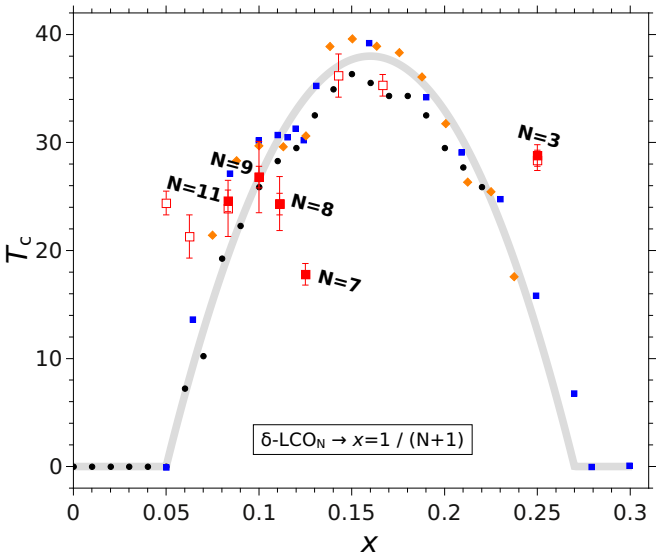

FIG. 5. Bulk phase diagram: T_c versus Sr doping for $La_{2-x}Sr_xCuO_4$. Black points are from Ref. [35], blue points are from Ref. [36], and orange points are from Ref. [37]. Red closed symbols are the T_c values plotted against the *formal* doping level $x = 1/(N+1)$ of the investigated samples. Open red symbols are from δ-LCO_N samples from Ref. [10].

APPENDIX B: μSR AND LE-μSR

In order to study the magnetic and superconducting properties of these δ-LCO_N superlattices we utilized the low-energy

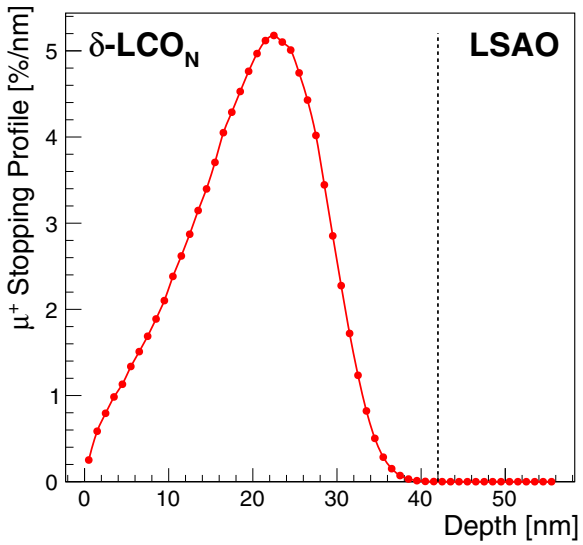

FIG. 6. The μ^+ stopping profile for an implantation energy of $E = 4$ keV in δ-LCO$_N$, calculated with TRIM.SP.

muon spectrometer at the μE4 beam line of the Paul Scherrer Institut in Switzerland [38].

μSR utilizes polarized positive muons (μ^+). Implanted into the sample, they thermalize within $\lesssim$10 ps and act as local magnetic probes in the host material. Bulk μSR uses energetic ($\sim$4 MeV) muons originating from π^+ decay at rest ("surface" muons) [39]. The μ^+ stopping range and straggling are on the submillimeter scale in a solid; hence, they are suitable for bulk studies.

Low-energy μSR makes use of epithermal muons ($\sim$15 eV) which are generated by moderation of surface muons in a thin film of a weakly bound van der Waals cryosolid (wide-band-gap insulator) [40,41]. By reaccelerating the epithermal muons up to 20 keV and biasing the sample, it is possible to tune the implantation energy in the range of 0.5 to 30 keV and thus to implant the muons beneath the surface of any material in a range of up to about 300 nm. The stopping range profiles are calculated by the Monte Carlo program TRIM.SP, which treats the positive muon as a light proton [42,43].

The stopping profile for the δ-LCO$_N$ samples is shown in Fig. 6.

1. Time evolution of the muon spin polarization

In a μSR experiment, a few million spin-polarized muons are implanted one at a time into a sample. The muon spin evolution of the ensemble is then measured as a function of time. The evolution can be monitored by utilizing the fact that the parity-violating radioactive muon decay is highly anisotropic with the easily detectable positron emitted preferentially in the direction of the μ^+ spin at the moment of the decay.

Counting the variation of the decay positron intensity $N(t)$ with one or more detectors as a function of time after the muon has stopped in the sample, it is possible to determine $P(t)$, the time dependence of the polarization along the initial muon spin direction.

The experimentally obtained time histograms have the form

$$N(t) = N_0\, e^{-t/\tau_\mu}\left[1 + A_0\,\frac{P(t)}{P(0)}\right] + N_{\rm bkg}. \qquad \text{(B1)}$$

N_0 is a normalization constant reflecting the scale of the recorded positrons. The exponent describes the decay of the μ^+ with the muon mean lifetime τ_μ. $N_{\rm bkg}$ is a time-independent background of uncorrelated positron events. A_0 is the maximum observable asymmetry which depends on the solid angle of the detector system and also on the implantation energy due to backscattering of muons. $A_0(E)$ is known from calibration experiments on Ag. The relevant information about the system under consideration is contained in the term $A_0\, P(t)/P(0)$.

a. Zero-field polarization function

Measured LE-μSR time spectra under zero-magnetic-field conditions were analyzed with the polarization function

$$\begin{aligned} A_0\,\frac{P(t)}{P(0)}\bigg|_{\rm ZF} &= A_1\left\{\frac{1}{3} + \frac{2}{3}[1-(\Delta_{\rm GKT}t)^2]\right. \\ &\quad \left.\times\,\exp\left[-\frac{1}{2}(\Delta_{\rm GKT}t)^2\right]\right\} e^{-\Lambda t} \\ &\quad + A_{\rm osc}\, j_0(\gamma_\mu B_{\rm int} t + \phi)\, e^{-(\sigma_{\rm osc}t)^2/2} \\ &\quad + \underbrace{A_{\rm F}\, e^{-\lambda_{\rm F} t} + A_{\text{Ni-tail}}}_{\text{Ni Bkg contribution}}. \end{aligned} \qquad \text{(B2)}$$

The first term in Eq. (B2) is the product of a Gaussian Kubo-Toyabe (GKT) function [26] and an exponent. The GKT function describes the nuclear depolarization in the paramagnetic state, where $\Delta_{\rm GKT}$ is the width of the static nuclear field distribution. The exponent Λ describes the gradual change over from the paramagnetic to the low-temperature magnetic state. The second term describes the zero-field precession signal of the antiferromagnetic state. The observed precession signal is better described by a zero-order spherical Bessel function than by a cosine in both phase and amplitude. This could indicate that the antiferromagnetic ground state shows some kind of modulation. One possibility could be the presence of *small* domains. γ_μ is the muon gyromagnetic ratio. $B_{\rm int}$ is the magnetic field measured at the muon site which, for $La_{2-x}Sr_xCuO_4$, is proportional to the sublattice magnetization of the antiferromagnetic state. The width of the magnetic field distribution of the ordered state is described by $\sigma_{\rm osc}$. Since the sample is mounted on a nickel-plated aluminum sample holder and some muons are missing the sample ($<$20%), a background contribution is present. This is described by the last term in Eq. (B2). It has been shown [44] that $A_{\rm F}$, $A_{\text{Ni-tail}}$, and $\lambda_{\rm F}$ are temperature independent, and $\lambda_{\rm F} \gtrsim 20\,\mu{\rm s}^{-1}$. Hence, only the first $\approx$0.05 μs are distorted by a time-dependent background.

b. Transverse field polarization function

To obtain the magnetic volume fraction and to study the vortex state in the superconducting phase, transverse field μSR experiments were carried out. For this case the muon spin

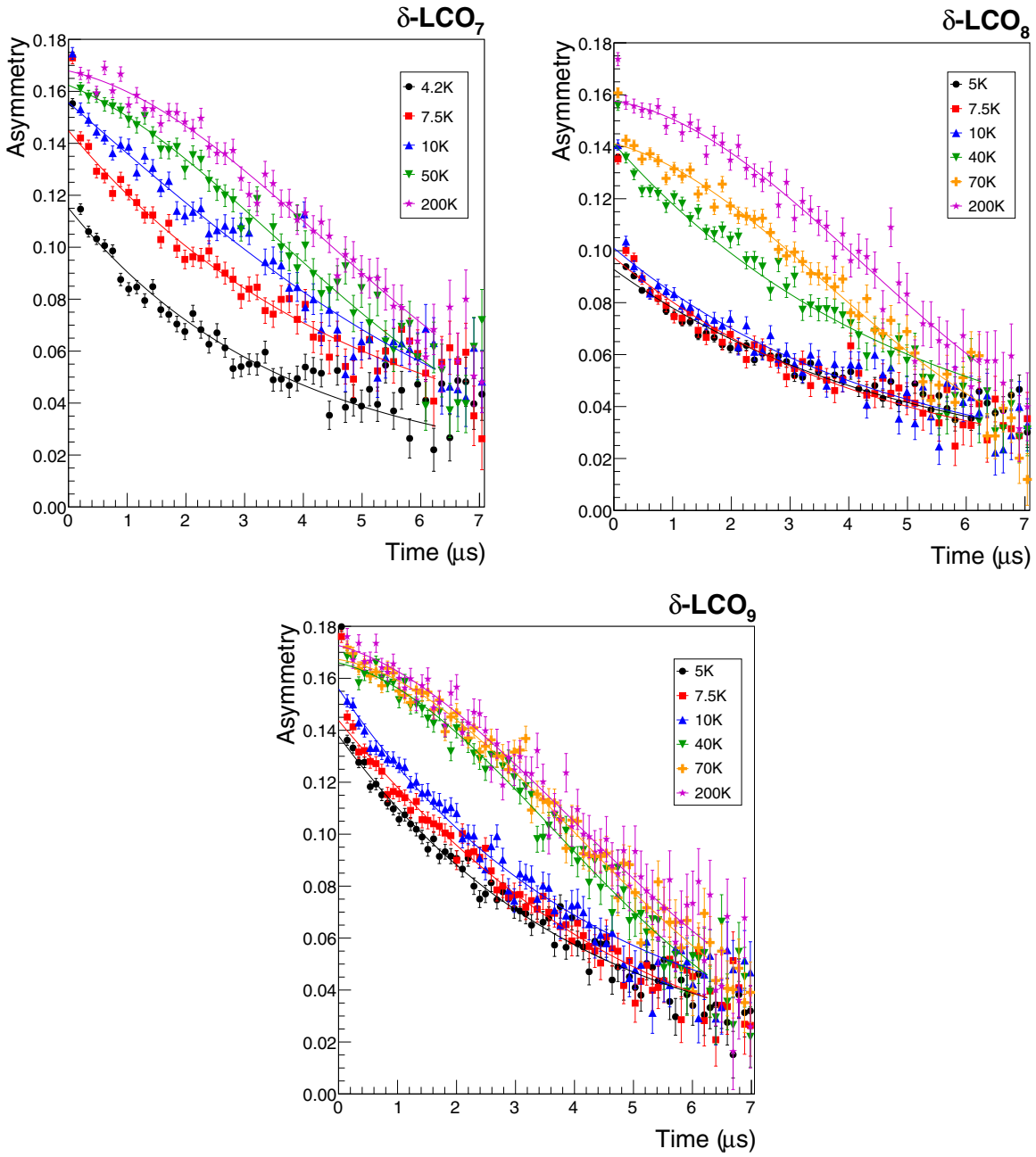

FIG. 7. Zero-field time spectra of the asymmetry, $A(t) = A_0 P(t)/P(0)$, of the δ-LCO$_N$ superlattices, measured at various temperatures.

polarization function can be written as

$$\left.\frac{P(t)}{P(0)}\right|_{\mathrm{TF}} = \int d^3B \left\{ \left(\frac{B_\parallel}{B}\right)^2 + \left(\frac{B_\perp}{B}\right)^2 \cos(\gamma_\mu B t) \right\}, \quad \text{(B3)}$$

where $B_\parallel^2 + B_\perp^2 = B^2$ and $B_{\parallel,\perp}$ are the field components parallel and perpendicular to the initial muon spin, respectively. Let's consider the case of a paramagnetic or superconducting state. In this case the dominant field will be the applied one, i.e., $B_\parallel \simeq 0$ and $B_\perp \simeq B_{\mathrm{ext}}$. Hence, $P(t)/P(0)$ will be the Fourier transform of the magnetic field distribution. In the superconducting state this will lead to a damping σ of the muon polarization function; σ can directly be related to the London penetration depth [15].

In the case of a magnetic ground state, B will be the superposition of the applied field $B_{\mathrm{ext}} = \mu_0 H_{\mathrm{ext}}$, which is applied perpendicular to the initial muon spin, and the internal field distribution. For this situation, both terms in Eq. (B3) will contribute. If $B_{\mathrm{ext}} \ll B_{\mathrm{int}}$, where B_{int} is the internal field, $P(t)/P(0)$ will show an extremely strong initial damping due to the symmetry breaking B_{ext}. This means that the precession amplitude will be strongly suppressed if the whole sample volume is homogeneously magnetic, or in other words, the loss of polarization is a direct measure of the magnetic volume fraction. For more details see Ref. [45].

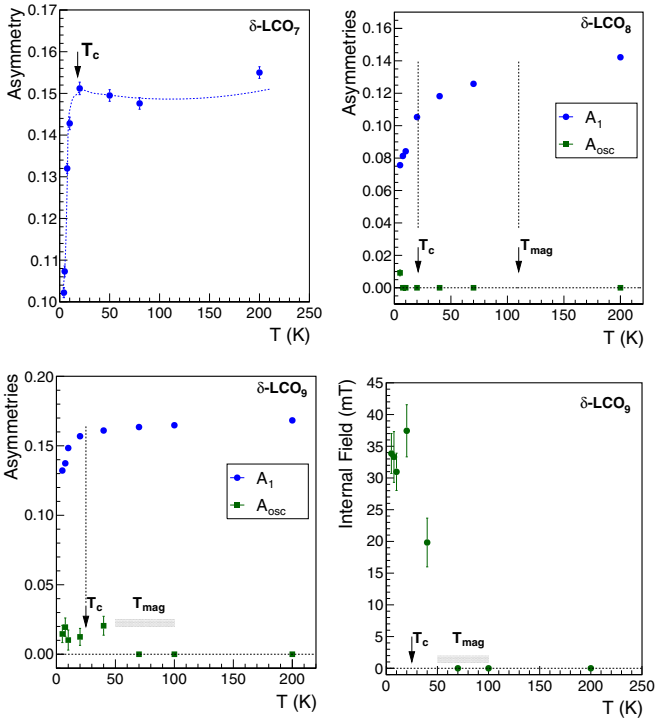

FIG. 8. Temperature dependence of the zero-field asymmetries $A(t=0,T)$ of the δ-LCO$_N$ superlattices. Top left: δ-LCO$_7$; top right: δ-LCO$_8$; bottom left: δ-LCO$_9$; bottom right: measured internal field at the muon site of δ-LCO$_9$. For δ-LCO$_9$ it was very hard to precisely determine $T_{\rm mag}$. Therefore, instead of an arrow, a shaded box is given as a crude-estimate region for $T_{\rm mag}$. The blue points and green squares show the temperature dependence of A_1 and $A_{\rm osc}$ [see Eq. (B2)], respectively.

The transverse field muon polarization function used is

$$A_0 \frac{P(t)}{P(0)}\bigg|_{\rm TF} = \underbrace{A_{\rm T}\exp(-\sigma^2 t^2/2)\cos(\gamma_\mu B_{\rm ext} t+\phi)}_{\text{paramag. part}} + \underbrace{A_{\rm L}\cos(\phi)}_{\text{TF-tail}}. \tag{B4}$$

Applying a small external magnetic field $B_{\rm ext} \ll B_{\rm int}$, fitting only the paramagnetic fraction, i.e., $B = B_{\rm ext}$, and ignoring the initial strongly damped part of $P(t)/P(0)$, the magnetic volume faction $f_{\rm M}$ can be determined as

$$f_{\rm M} = 1 - A_{\rm T}/A_0 \tag{B5}$$

As a crosscheck, $A_{\rm L}$ should start to grow at the magnetic transition $T_{\rm mag}$ when the temperature is lowered.

Applying a strong external magnetic field $B_{\rm ext} \gg B_{\rm int}$ and again fitting only the paramagnetic fraction, the damping σ will reflect the broadening due to the vortex state. To be more precise [15],

$$\left(\frac{\sigma_{\rm sc}}{\gamma_\mu}\right)^2 = 0.00371\,\frac{\Phi_0^2}{\lambda^4}, \tag{B6}$$

where $\sigma_{\rm sc} = \sqrt{\sigma(T)^2 - \sigma(T>T_c)^2}$, $\Phi_0 = 2.067 \times 10^{-15}\,(\mathrm{T\,m^2})$ is the flux quantum, and λ is the magnetic penetration depth.

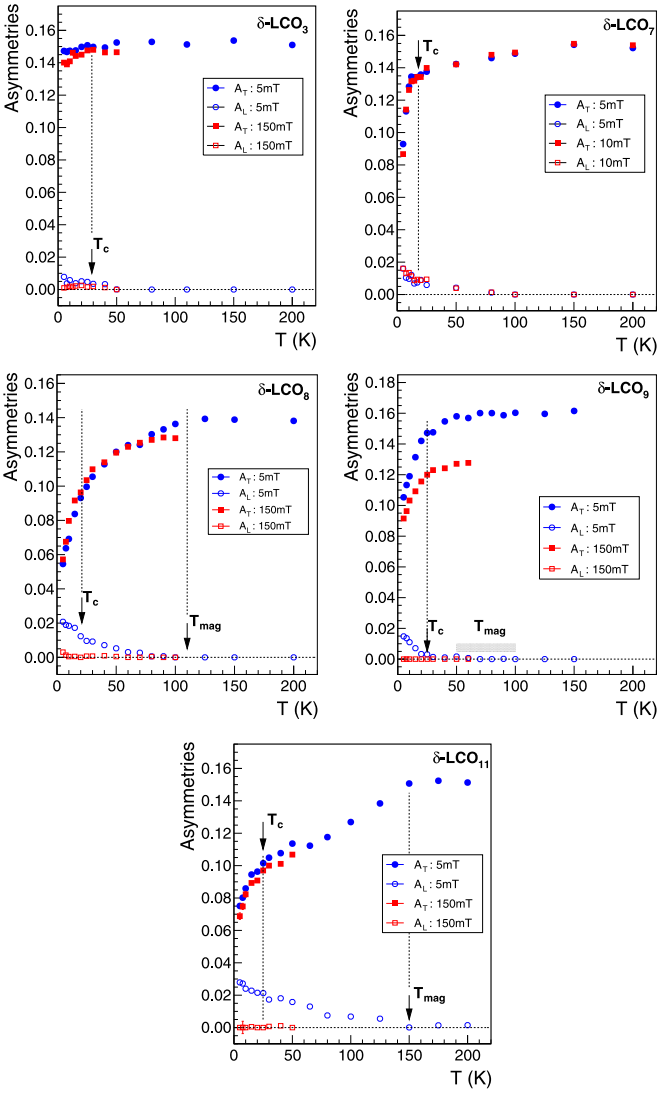

FIG. 9. Temperature dependence of the transverse field asymmetries for $H_{\rm ext}$ perpendicular to the δ-LCO$_N$ superlattice layers. $A_{\rm T}$ and $A_{\rm L}$ are as defined in Sec. B 1 b, Eq. (B4). Note the expected suppression of $A_{\rm L}$ for high applied magnetic fields, i.e., $\mu_0 H_{\rm ext} \gg B_{\rm int}$.

In the Meissner state, after zero-field cooling and applying a magnetic field $H_{\rm ext} < H_{c1}$, the magnetic field penetrates the superconductor from the surface and decays exponentially as

$$B(z) = \mu_0 H_{\rm ext}\exp[-z/\lambda(T)], \tag{B7}$$

where $\mu_0 = 4\pi \times 10^{-7}\mathrm{H/m}$, z is the distance from the surface, and $\lambda(T)$ is the magnetic penetration depth. Since we are discussing thin-film properties, it is assumed that for the Meissner screening measurements $H_{\rm ext}$ is applied parallel to the film surface. For a thin film with thickness $d < \lambda(T)$, the magnetic screening profile will take the form

$$B(z) = \mu_0 H_{\rm ext}\frac{\cosh[(d/2-z)/\lambda(T)]}{\cosh[d/(2\lambda(T))]} \tag{B8}$$

since the magnetic field can penetrate from both sides. Different from the vortex state where the depolarization rate σ is a measure of the magnetic field distribution, in the Meissner state

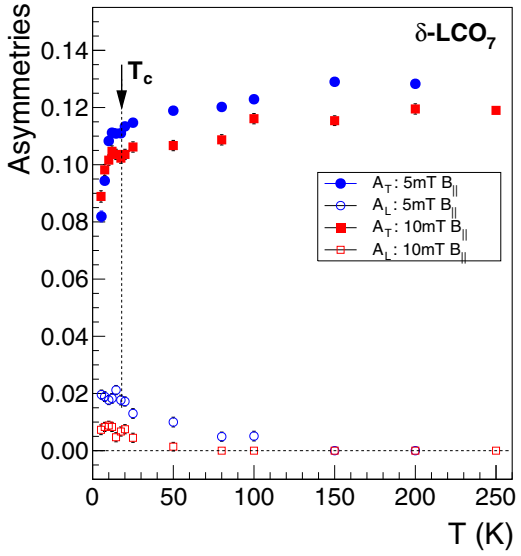

FIG. 10. Temperature dependence of the transverse field asymmetries for $H_{\rm ext} \lesssim H_{c1}$ parallel to the δ-LCO_7 superlattice layers. The magnetic volume fraction $f_{\rm M}$ [see Eq. (B5)] obtained from this geometry corresponds, within the error bars, to the one obtained from the perpendicular geometry. This demonstrates that potential magnetic vortex states cannot be the cause of trends shown in Fig. 4.

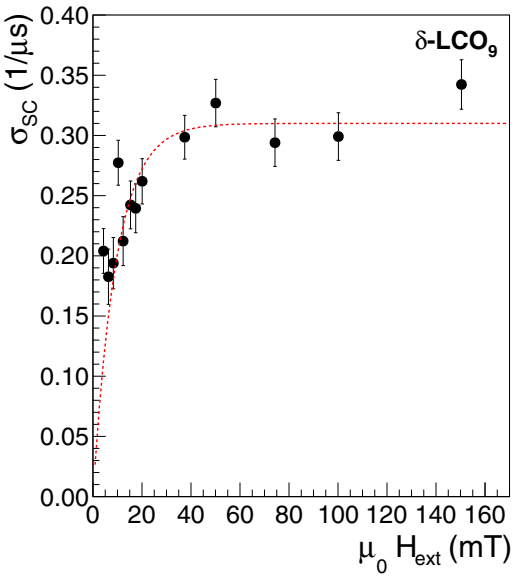

FIG. 11. Field dependence of $\sigma_{\rm SC} = \sqrt{\sigma^2(T = 8\ {\rm K}) - \sigma^2(T = 35\ {\rm K})}$ for δ-LCO_9 after FC. The field was applied perpendicular to the film, i.e., out of plane. The red dashed line is a guide to the eye. $\sigma_{\rm SC}$ is essentially field independent for $\mu_0 H_{\rm ext} > 40$ mT, which allows us to use Eq. (1) to determine $\lambda_{\rm L}$.

the angular frequency $\bar{\omega}(T) = \int dz\, \{n(z)\, \gamma_\mu B(z)\} / \int dz\, n(z)$ can be used to map out $B(z)$ according to Eqs. (B7) and (B8), where $n(z)$ is the muon stopping distribution. For further details see Ref. [46].

All μSR data were analyzed using the MUSRFIT framework [47].

APPENDIX C: ZERO-FIELD LE-μSR DATA OF THE δ-LCO_N SUPERLATTICES

The zero-field time spectra of the δ-LCO_N superlattices are shown in Fig. 7.

The temperature dependencies of the δ-LCO_N superlattice asymmetries $A(t = 0)$ are given in Fig. 8.

APPENDIX D: TRANSVERSE FIELD LE-μSR DATA OF THE δ-LCO_N SUPERLATTICES

The temperature dependencies of the δ-LCO_N superlattice asymmetries, obtained from transverse field measurements and $H_{\rm ext}$ perpendicular to the superlattice layers, are given in Fig. 9. $A_{\rm T}$ and $A_{\rm L}$ are defined in Eq. (B4). Figure 10 shows the corresponding data for $H_{\rm ext}$ parallel to the superlattice layers. Figure 11 shows the field dependence of $\sigma_{\rm sc} = \sqrt{\sigma^2(T = 8\,{\rm K}) - \sigma^2(T = 35\,{\rm K})}$ for δ-LCO_9. As can be seen, the value of $\sigma_{\rm sc}$ saturates for $\mu_0 H_{\rm ext} > 40$ mT. All the measurements used to determine $\sigma_{\rm sc}$ were carried out at $\mu_0 H_{\rm ext} = 150$ mT.

[1] B. Keimer, S. A. Kivelson, M. R. Norman, S. Uchida, and J. Zaanen, From quantum matter to high-temperature superconductivity in copper oxides, Nature (London) **518**, 179 (2015).

[2] J. M. Tranquada, B. J. Sternlieb, J. D. Axe, Y. Nakamura, and S. Uchida, Evidence for stripe correlations of spins and holes in copper oxide superconductors, Nature (London) **375**, 561 (1995).

[3] H.-H. Klauss, Spin stripe order and superconductivity in layered transition metal oxides, J. Phys.: Condens. Matter **16**, S4457 (2004).

[4] P. Corboz, T. M. Rice, and M. Troyer, Competing States in the t-J Model: Uniform d-Wave State Versus Stripe State, Phys. Rev. Lett. **113**, 046402 (2014).

[5] B. M. Andersen, S. Graser, and P. J. Hirschfeld, Disorder-Induced Freezing of Dynamical Spin Fluctuations in Underdoped Cuprate Superconductors, Phys. Rev. Lett. **105**, 147002 (2010).

[6] B. O. Wells, Incommensurate spin fluctuations in high-transition temperature superconductors, Science **277**, 1067 (1997).

[7] H. E. Mohottala, B. O. Wells, J. I. Budnick, W. A. Hines, C. Niedermayer, L. Udby, C. Bernhard, A. R. Moodenbaugh, and F.-C. Chou, Phase separation in superoxygenated $La_{2-x}Sr_xCuO_{4+y}$, Nat. Mater. **5**, 377 (2006).

[8] M. Fratini, N. Poccia, A. Ricci, G. Campi, M. Burghammer, G. Aeppli, and A. Bianconi, Scale-free structural organization of oxygen interstitials in La_2CuO_{4+y}, Nature (London) **466**, 841 (2010).

[9] L. Udby, J. Larsen, N. B. Christensen, M. Boehm, Ch. Niedermayer, H. E. Mohottala, T. B. S. Jensen, R. Toft-Petersen, F. C. Chou, N. H. Andersen, K. Lefmann, and B. O. Wells, Measurement of Unique Magnetic and Superconducting Phases in Oxygen-Doped High-Temperature Superconductors $La_{2-x}Sr_xCuO_{4+y}$, Phys. Rev. Lett. **111**, 227001 (2013).

[10] F. Baiutti, G. Logvenov, G. Gregori, G. Cristiani, Y. Wang, W. Sigle, P. A. van Aken, and J. Maier, High-temperature superconductivity in space-charge regions of lanthanum cuprate induced by two-dimensional doping, Nat. Commun. **6**, 8586 (2015).

[11] Yi Wang, F. Baiutti, G. Gregori, G. Cristiani, U. Salzberger, G. Logvenov, J. Maier, and P. A. van Aken, Atomic-Scale Quantitative Analysis of Lattice Distortions at Interfaces of Two-Dimensionally Sr-Doped La_2CuO_4 Superlattices, ACS Appl. Mater. Interfaces **8**, 6763 (2016).

[12] B. Keimer, A. Aharony, A. Auerbach, R. J. Birgeneau, A. Cassanho, Y. Endoh, R. W. Erwin, M. A. Kastner, and G. Shirane, Néel transition and sublattice magnetization of pure and doped La_2CuO_4, Phys. Rev. B **45**, 7430 (1992).

[13] Y. J. Uemura, V. J. Emery, A. R. Moodenbaugh, M. Suenaga, D. C. Johnston, A. J. Jacobson, J. T. Lewandowski, J. H. Brewer, R. F. Kiefl, S. R. Kreitzman, G. M. Luke, T. Riseman, C. E. Stronach, W. J. Kossler, J. R. Kempton, X. H. Yu, D. Opie, and H. E. Schone, Systematic variation of magnetic-field penetration depth in high-T_c superconductors studied by muon-spin relaxation, Phys. Rev. B **38**, 909 (1988).

[14] E. Morenzoni, T. Prokscha, A. Suter, H. Luetkens, and R. Khasanov, Nano-scale thin film investigations with slow polarized muons, J. Phys.: Condens. Matter **16**, S4583 (2004).

[15] E. H. Brandt, Flux distribution and penetration depth measured by muon spin rotation in high-T_c superconductors, Phys. Rev. B **37**, 2349 (1988).

[16] E. H. Brandt, Properties of the ideal Ginzburg-Landau vortex lattice, Phys. Rev. B **68**, 054506 (2003).

[17] J. R. Clem, Two-dimensional vortices in a stack of thin superconducting films: A model for high-temperature superconducting multilayers, Phys. Rev. B **43**, 7837 (1991).

[18] Determining H_{c1} for these superlattices is not straightforward. Assuming a full-volume superconducting state, we estimate $H_{c1} = \Phi_0/(4\pi\lambda_L^2)\ln(\lambda_L/\xi) \simeq 10$ mT. This should be a lower-limit estimate since for a film with a thickness $d < \lambda_L$ there is an additional H_{c1} enhancement compared to the above estimate [48].

[19] V. M. Loktev and Yu. G. Pogorelov, Model for modulated electronic configurations in selectively doped multilayered La_2CuO_4 nanostructures, Phys. Rev. B **78**, 180501(R) (2008).

[20] A. Suter, E. Morenzoni, T. Prokscha, H. Luetkens, B. M. Wojek, G. Logvenov, A. Gozar, and I. Božovič, Superconductivity in $La_{1.56}Sr_{0.44}CUO_4/La_2CUO_4$ Superlattices, Phys. Procedia **30**, 271 (2012).

[21] A. Ino, T. Mizokawa, A. Fujimori, K. Tamasaku, H. Eisaki, S. Uchida, T. Kimura, T. Sasagawa, and K. Kishio, Chemical Potential Shift in Overdoped and Underdoped $La_{2-x}Sr_xCuO_4$, Phys. Rev. Lett. **79**, 2101 (1997).

[22] P. J. Baker, T. Lancaster, S. J. Blundell, F. L. Pratt, M. L. Brooks, and S.-J. Kwon, Tuning the Interlayer Spacing of High-T_c Bi-Based Superconductors by Intercalation: Measuring the Penetration Depth and the Two-Dimensional Superfluid Density, Phys. Rev. Lett. **102**, 087002 (2009).

[23] A. Boris *et al.* (unpublished).

[24] H. Luetkens, H.-H. Klauss, R. Khasanov, A. Amato, R. Klingeler, I. Hellmann, N. Leps, A. Kondrat, C. Hess, A. Kühler, G. Behr, J. Werner, and B. Büchner, Field and Temperature Dependence of the Superfluid Density in $LaFeAsO_{1-x}F_x$ Superconductors: A Muon Spin Relaxation Study, Phys. Rev. Lett. **101**, 097009 (2008).

[25] P. D. de Réotier and A Yaouanc, Muon spin rotation and relaxation in magnetic materials, J. Phys.: Condens. Matter **9**, 9113 (1997).

[26] A. le Yaouanc and P. D. Dalmas de Réotier, *Muon Spin Rotation, Relaxation, and Resonance: Applications to Condensed Matter*, International Series of Monographs on Physics Vol. 147 (Oxford University Press, Oxford, 2010).

[27] F. Borsa, P. Carretta, J. H. Cho, F. C. Chou, Q. Hu, D. C. Johnston, A. Lascialfari, D. R. Torgeson, R. J. Gooding, N. M. Salem, and K. J. E. Vos, Staggered magnetization in $La_{2-x}Sr_xCuO_4$ from ^{139}La NQR and μSR: Effects of Sr doping in the range $0 < x < 0.02$, Phys. Rev. B **52**, 7334 (1995).

[28] A. T. Savici, Y. Fudamoto, I. M. Gat, T. Ito, M. I. Larkin, Y. J. Uemura, G. M. Luke, K. M. Kojima, Y. S. Lee, M. A. Kastner, R. J. Birgeneau, and K. Yamada, Muon spin relaxation studies of incommensurate magnetism and superconductivity in stage-4 $La_2CuO_{4.11}$ and $La_{1.88}Sr_{0.12}CuO_4$, Phys. Rev. B **66**, 014524 (2002).

[29] C. Bernhard, C. N. Wang, L. Nuccio, L. Schulz, O. Zaharko, J. Larsen, C. Aristizabal, M. Willis, A. J. Drew, G. D. Varma, T. Wolf, and Ch. Niedermayer, Muon spin rotation study of magnetism and superconductivity in $Ba(Fe_{1-x}Co_x)_2As_2$ single crystals, Phys. Rev. B **86**, 184509 (2012).

[30] Z. Guguchia, R. Khasanov, M. Bendele, E. Pomjakushina, K. Conder, A. Shengelaya, and H. Keller, Negative Oxygen Isotope Effect on the Static Spin Stripe Order in Superconducting $La_{2-x}Ba_xCuO_4(x = 1/8)$ Observed by Muon-Spin Rotation, Phys. Rev. Lett. **113**, 057002 (2014).

[31] S. A. Kivelson, G. Aeppli, and V. J. Emery, Thermodynamics of the interplay between magnetism and high-temperature superconductivity, Proc. Natl. Acad. Sci. USA **98**, 11903 (2001).

[32] D. I. Khomskii and F. V. Kusmartsev, Charge redistribution and properties of high-temperature superconductors, Phys. Rev. B **46**, 14245 (1992).

[33] A. Charnukha, P. Popovich, Y. Matiks, D. L. Sun, C. T. Lin, A. N. Yaresko, B. Keimer, and A. V. Boris, Superconductivity-induced optical anomaly in an iron arsenide, Nat. Commun. **2**, 219 (2010).

[34] F. Baiutti, G. Gregori, Y. Wang, Y. E. Suyolcu, G. Cristiani, P. A. van Aken, J. Maier, and G. Logvenov, Cationic redistribution at epitaxial interfaces in superconducting two-dimensionally doped lanthanum cuprate films, ACS Appl. Mater. Interfaces **8**, 27368 (2016).

[35] Y. Ando, S. Komiya, K. Segawa, S. Ono, and Y. Kurita, Electronic Phase Diagram of High-T_c Cuprate Superconductors from a Mapping of the In-Plane Resistivity Curvature, Phys. Rev. Lett. **93**, 267001 (2004).

[36] T. Nagano, Y. Tomioka, Y. Nakayama, K. Kishio, and K. Kitazawa, Bulk superconductivity in both tetragonal and orthorhombic solid solutions of $(La_{1-x}Sr_x)_2CuO_{4-\delta}$, Phys. Rev. B **48**, 9689 (1993).

[37] P. G. Radaelli, D. G. Hinks, A. W. Mitchell, B. A. Hunter, J. L. Wagner, B. Dabrowski, K. G. Vandervoort, H. K. Viswanathan, and J. D. Jorgensen, Structural and superconducting properties of $La_{2-x}Sr_xCuO_4$ as a function of Sr content, Phys. Rev. B **49**, 4163 (1994).

[38] T. Prokscha, E. Morenzoni, K. Deiters, F. Foroughi, D. George, R. Kobler, A. Suter, and V. Vrankovic, The new beam at PSI: A hybrid-type large acceptance channel for the generation of a high intensity surface-muon beam, Nucl. Instrum. Methods Phys. Res., Sect. A **595**, 317 (2008).

[39] A. G. Schenck, *Muon Spin Rotation Spectroscopy: Principles and Applications in Solid State Physics* (Hilger, Bristol, 1985).

[40] D. R. Harshman, A. P. Mills, J. L. Beveridge, K. R. Kendall, G. D. Morris, M. Senba, J. B. Warren, A. S. Rupaal, and J. H. Turner, Generation of slow positive muons from solid rare-gas moderators, Phys. Rev. B **36**, 8850 (1987).

[41] E. Morenzoni, F. Kottmann, D. Maden, B. Matthias, M. Meyberg, Th. Prokscha, Th. Wutzke, and U. Zimmermann, Generation of Very Slow Polarized Positive Muons, Phys. Rev. Lett. **72**, 2793 (1994).

[42] W. Eckstein, *Computer Simulation of Ion-Solid Interactions* (Springer, Berlin, 1991).

[43] E. Morenzoni, H. Glückler, T. Prokscha, R. Khasanov, H. Luetkens, M. Birke, E. M. Forgan, Ch. Niedermayer, and M. Pleines, Implantation studies of keV positive muons in thin metallic layers, Nucl. Instrum. Methods Phys. Res., Sect. B **192**, 254 (2002).

[44] H. Saadaoui, Z. Salman, T. Prokscha, A. Suter, B. M. Wojek, and E. Morenzoni, Zero-field spin depolarization of low-energy muons in ferromagnetic nickel and silver metal, Phys. Proc. **30**, 164 (2012).

[45] F. L. Pratt, Field dependence of μSR signals in a polycrystalline magnet, J. Phys.: Condens. Matter **19**, 456207 (2007).

[46] R. F. Kiefl, M. D. Hossain, B. M. Wojek, S. R. Dunsiger, G. D. Morris, T. Prokscha, Z. Salman, J. Baglo, D. A. Bonn, R. Liang, W. N. Hardy, A. Suter, and E. Morenzoni, Direct measurement of the London penetration depth in $YBa_2Cu_3O_{6.92}$ using low-energy μSR, Phys. Rev. B **81**, 180502 (2010).

[47] A. Suter and B. M. Wojek, Musrfit: A Free Platform-Independent Framework for μSR Data Analysis, Phys. Procedia **30**, 69 (2012).

[48] M. Tinkham, *Introduction to Superconductivity* (McGraw-Hill, New York, 1975).